JACS
JOURNAL OF THE AMERICAN CHEMICAL SOCIETY
Article
pubs.acs.org/JACS

Molecular Insight in Structure and Activity of Highly Efficient, Low-Ir Ir−Ni Oxide Catalysts for Electrochemical Water Splitting (OER)

Tobias Reier,[*,†] Zarina Pawolek,[†] Serhiy Cherevko,[‡] Michael Bruns,[§] Travis Jones,[∥] Detre Teschner,[∥] Sören Selve,[⊥] Arno Bergmann,[†] Hong Nhan Nong,[†] Robert Schlögl,[∥] Karl J. J. Mayrhofer,[‡] and Peter Strasser[*,†]

[†]Department of Chemistry, Chemical and Materials Engineering Division, The Electrochemical Energy, Catalysis and Materials Science Laboratory, Technische Universität Berlin, Straße des 17. Juni 124, 10623 Berlin, Germany

[‡]Department of Interface Chemistry and Surface Engineering, Max-Planck-Institut für Eisenforschung GmbH, Max-Planck-Straße 1, 40237 Düsseldorf, Germany

[§]Institute for Applied Materials and Karlsruhe Nano Micro Facility, Karlsruhe Institute of Technology (KIT), Hermann-von-Helmholtz-Platz 1, D-76344 Eggenstein-Leopoldshafen, Germany

[∥]Department of Inorganic Chemistry, Fritz-Haber-Institute of the Max-Planck-Society, Faradayweg 4-6, 14195 Berlin, Germany

[⊥]Zentraleinrichtung Elektronenmikroskopie, Technische Universität Berlin, D-10623 Berlin, Germany

Supporting Information

ABSTRACT: Mixed bimetallic oxides offer great opportunities for a systematic tuning of electrocatalytic activity and stability. Here, we demonstrate the power of this strategy using well-defined thermally prepared Ir−Ni mixed oxide thin film catalysts for the electrochemical oxygen evolution reaction (OER) under highly corrosive conditions such as in acidic proton exchange membrane (PEM) electrolyzers and photoelectrochemical cells (PEC). Variation of the Ir to Ni ratio resulted in a volcano type OER activity curve with an unprecedented *20-fold improvement* in Ir mass-based activity over pure Ir oxide. In situ spectroscopic probing of metal dissolution indicated that, against common views, activity and stability are not directly anticorrelated. To uncover activity and stability controlling parameters, the Ir−Ni mixed thin oxide film catalysts were characterized by a wide array of spectroscopic, microscopic, scattering, and electrochemical techniques in conjunction with DFT theoretical computations. By means of an intuitive model for the formation of the catalytically active state of the bimetallic Ir−Ni oxide surface, we identify the coverage of reactive surface hydroxyl groups as a suitable descriptor for the OER activity and relate it to controllable synthetic parameters. Overall, our study highlights a novel, highly active oxygen evolution catalyst; moreover, it provides novel important insights into the structure and performance of bimetallic oxide OER electrocatalysts in corrosive acidic environments.

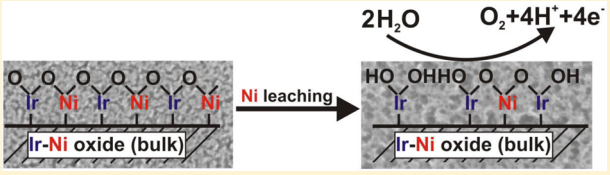

1. INTRODUCTION

Hydrogen production via water electrolysis is an emerging key technology for the long-term storage of electricity from renewable sources to mitigate their intermittent availability.[1] The low ohmic loss, low kinetic overpotential, and large partial load range provided by proton exchange membrane (PEM) electrolyzers make them the most promising technology in this regard.[2] However, the harsh corrosive acidic conditions in a PEM electrolyzer are demanding with respect to the catalysts stability and make the utilization of noble metals indispensable. Considering PEM electrolyzers, the main catalytic efficiency loss (overpotential) is related to the anode reaction, the oxygen evolution reaction (OER), due to a complex four electron reaction mechanism.[1,3] Therefore, improved anode catalysts combining high catalytic activity and sufficient corrosion stability at minimized noble metal content are required to facilitate the large scale application of PEM water electrolysis.

Ir oxide is one of the most appropriate PEM electrolyzer OER catalysts, combining excellent activity and stability.[4−7] Unfortunately, Ir is a very rare element with an abundance 10 times lower than Pt.[2] To make its application feasible on a large scale the Ir amount required must be reduced to a minimum. So far, approaches to lower the Ir content have focused mainly on dispersing Ir oxide. For instance, Ir oxide was dispersed on a conductive high surface area support[8] or in a mixture with one or more inert components, such as oxides of Ti,[6] Ta,[6] Nb,[9] Sb,[10] Sn,[11] or Si.[12] However, this approach alone is most likely not sufficient to achieve the required reduction of the Ir amount. Therefore, the intrinsic OER activity and stability of Ir oxide have to be tuned to a maximum. Unfortunately, the material properties determining the OER activity and stability of Ir oxide remain uncertain. To identify the relevant material properties, a system is required in which the OER activity and stability can be continuously varied. By tuning the OER activity and stability and assessing the consequent changes in the

Received: July 25, 2015
Published: September 10, 2015

ACS Publications © 2015 American Chemical Society

DOI: 10.1021/jacs.5b07788
J. Am. Chem. Soc. 2015, 137, 13031−13040

materials properties, one can uncover the governing structure-function correlations.

Ru oxide, which provides a slightly higher OER activity than Ir oxide, has been modified using Ni.[13,14] The Ru−Ni mixed oxide showed enhanced OER activity depending on the Ni content.[13] This was explained by Ni-rich defects in the Ru oxide lattice acting as preferential sites for the OER.[15] Unfortunately, Ru oxides suffer from severe corrosion under PEM-OER conditions,[16−19] rendering them unsuitable as stable OER catalysts. On the other hand, Nong et al. demonstrated that addition of Ni to Ir in form of electrochemically oxidized $IrNiO_x$ core−shell nanoparticles boosted the Ir utilization and the intrinsic Ir OER activity,[20,21] suggesting the great promise of this approach for a continuous variation of Ir oxide material properties. However, to fully unfold its potential, this approach has to be extended to thermally prepared Ir−Ni oxides, because only thermally prepared oxides provide the superior stability[22] required for PEM electrolyzers or photoelectrochemical cells (PECs).

Here, we present atomic-scale insights into the structure-activity-stability relations of a new class of thermally prepared bimetallic model Ir−Ni oxide thin film catalysts with tunable OER activity and stability. The Ir−Ni oxide films exhibit unparalleled water splitting OER activities up to a 20× improvement in Ir-mass based OER activity compared to a state-of-art Ir oxide reference catalyst. To understand their exceptional performance at the atomic scale, we probe surface and bulk chemical properties and correlate them with the electrocatalytic OER activity and stability. Using this approach, we identify experimental material descriptors determining the electrocatalytic OER activity and stability of the mixed Ir−Ni oxides. Further, we provide evidence that OER activity and stability does not strictly follow the long-held conjecture of a reciprocal relation, offering the prospect of their separate optimization.

2. EXPERIMENTAL SECTION

A short description of the main experimental details is provided below; further details are mentioned in the Supporting Information (SI).

Film Preparation. Thin precursor films were applied onto the substrates (polished Ti cylinders or, for SAED and cross section SEM, Si wafers) by spin coating (WS-650MZ-23NPP, Laurell). Custom made sample holders, providing a bigger coated surface area, were used for Ti cylinders to minimize boundary effects. Coating solutions with 80 g L^{-1} Ir(III) acetate (99.95%, Chempur) or 105 g L^{-1} Ni(II) acetate tetrahydrate (99.998%, Sigma-Aldrich) in ethanol (abs., AnalaR Normapur) were mixed to obtain the desired Ir:Ni ratios. The solutions were applied onto the spinning substrate at 200 rpm ensuring full coverage. Accordingly, the rotation velocity was increased to 2000 rpm with 200 revolutions s^{-2} and dwelled at this velocity for 45 s to finish the spin coating process. The coated samples were calcined in a preheated muffle furnace (Carbolite) at 450 °C for 15 min. Film composition and loading (Ir and Ni) were determined by ICP-OES. Therefore, uncalcined films were dissolved in water. Ir−Ni mixed oxide catalysts will be referred to as x%Ni-MO (MO for Ir−Ni mixed oxide). Thereby, x specifies the Ni content in atomic % (at%) ($x = c(\mathrm{Ni})/(c(\mathrm{Ni}) + c(\mathrm{Ir}))$) in the as-prepared mixed oxide. Similarly, all Ni contents used to specify a certain mixed oxide sample are provided in at% and refer to the as-prepared state. To point out whether as prepared or OER tested samples were actually measured, as prepared samples will be referred to as x%Ni-MO-ap whereas the OER tested samples will be referred to as x%Ni-MO-OER.

Electrochemical Measurements (OER Protocol). The electrochemical measurements were performed at room temperature in a rotating disk electrode (RDE) setup equipped with a three compartment electrochemical glass cell including a Luggin capillary, rotator (Pine research instrumentation), and a potentiostat (SP-200, BioLogic).[23] A Hg/Hg_2SO_4 reference electrode and a Pt mesh counter electrode were applied. The reference electrode was calibrated against a reversible hydrogen electrode (RHE) in the same electrolyte. All potentials provided in this article were converted and referred to the RHE.

The samples were immersed at 1.2 V_{RHE} into the nitrogen degassed (15 min) electrolyte (0.1 M $HClO_4$), followed by three scans into the OER potential region. The first and third scan were measured with 6 mV s^{-1}, whereas the second scan was a quasi-stationary potential step scan with a step size of 20 mV and a dwell time of 5 min per step. We note that given the dwell time any sort of solid state bulk diffusion processes that may be beneficial or detrimental to the catalyst performance or stability are inherently not considered in this study. The ohmic drop was determined by impedance spectroscopy after every step and was used for iR correction. Subsequently, after a second N_2 degassing, cyclic voltammetry was measured as described in the SI. Thereafter, again three OER scans were performed (conditions as described before) of which the quasi-stationary one was used to evaluate the OER activity here. Three samples were measured for each MO composition. The average value and standard deviation obtained from these three measurements were used to express the OER activity and the related confidence range. The OER measurements were performed with a RDE rotation speed of 1600 rpm while the cyclic voltammetry was conducted with 0 rpm.

Potential-Resolved Inductively Coupled Plasma Mass Spectrometry (ICP-MS). Time- and potential-resolved analysis of dissolution products was carried out with a scanning flow cell (SFC) based setup.[18,22] MO-OER served as working electrodes. An Ag/AgCl reference electrode and a graphite rod counter electrode were applied. The potential was controlled by a potentiostat (Reference 600, Gamry). During the measurement, the electrolyte (0.1 M $HClO_4$) was pumped with a constant flow rate of ca. 180 μL min^{-1} through the flow cell and further downstream into an ICP-MS (NexION 300X, PerkinElmer). For the measurement, the current was stepped from open circuit potential (0 mA cm^{-2}) to 1 mA cm^{-2} for 30 min, while the dissolution rates of Ir and Ni were monitored.

Inductively Coupled Plasma Atomic Emission Spectroscopy (ICP-OES). ICP-OES was measured with a Varian 715-ES ICP instrument.

Scanning Electron Microscopy (SEM). SEM images were acquired in secondary electron mode with a JEOL 7401F field emission scanning electron microscope operated at 10 kV. The images were filtered.

Selected Area Electron Diffraction (SAED). SAED was measured with 200 kV in a FEI TECNAI G^2 20 S-TWIN instrument equipped with LaB_6 cathode and GATAN MS794 P CCD camera. The diffraction images were integrated, and the data were transferred into the 2θ scale (Cu Kα). The background was fitted with a double exponential decay function and subtracted.

X-ray Absorption Spectroscopy (XAS). O K-edge absorption spectra recorded in the total electron yield mode were collected at the ISISS beamline of the synchrotron radiation facility BESSY of the Helmholtz-Zentrum Berlin (HZB).

X-ray Photoelectron Spectroscopy (XPS). XPS measurements were performed using a K-Alpha XPS spectrometer (Thermo Fisher Scientific).

Density Functional Theory (DFT). All DFT calculations were performed using the Quantum ESPRESSO package.[24]

3. RESULTS AND DISCUSSION

At the outset of this study seven Ir−Ni mixed oxide thin film catalysts were prepared, ranging from 0 atomic % (at%) Ni to 100 at% Ni in composition. The films were well-defined regarding thickness and morphology using a spin-coating process validated previously.[25] For convenience and clarity in the following, Ir−Ni mixed oxide catalysts will be referred to as x%Ni-MO (MO for Ir−Ni mixed oxide). Thereby, x specifies

DOI: 10.1021/jacs.5b07788
J. Am. Chem. Soc. 2015, 137, 13031−13040

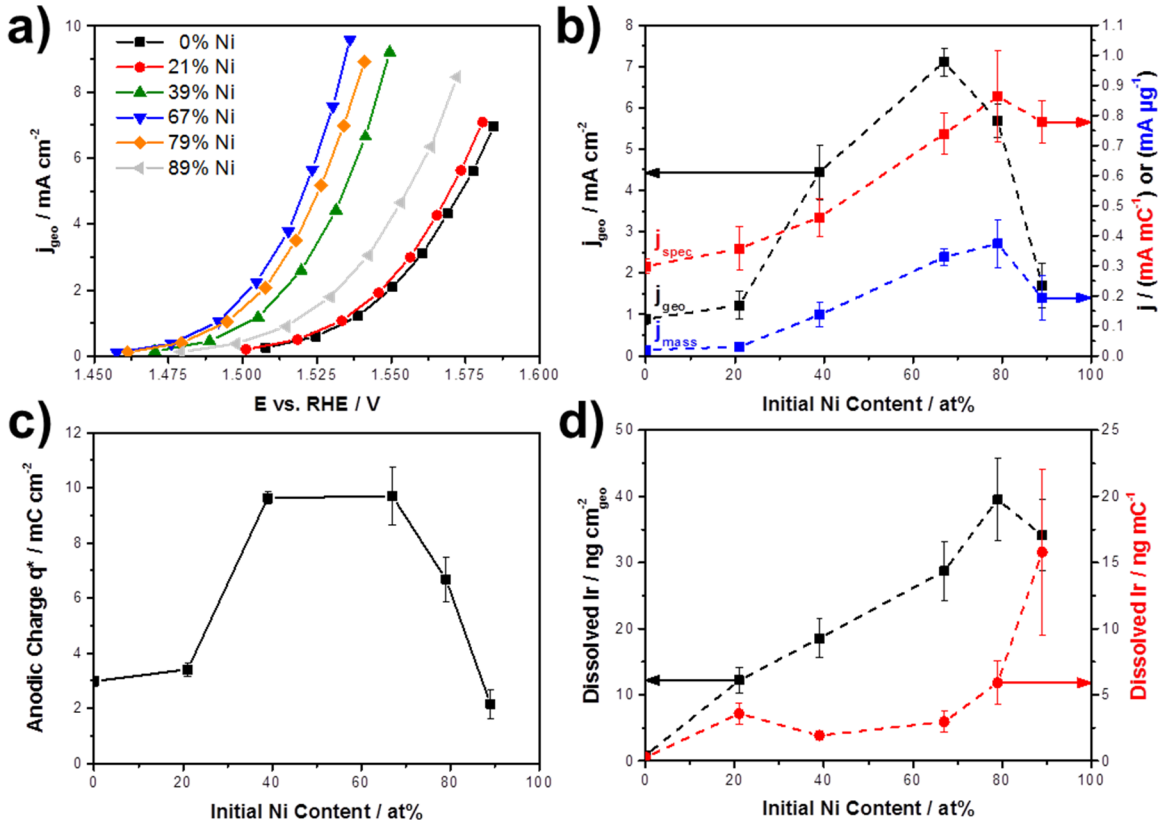

Figure 1. Electrocatalytic measurements of OER activity and stability of Ir–Ni mixed oxide films with different Ir to Ni ratios, here referred to as *x*% Ni-MO (*x* at% Ni). (a) Quasi-stationary OER polarization curves (*iR* corrected). (b) Current densities at an OER overpotential of 300 mV (1.530 V vs RHE) normalized to the electrodes geometric surface area (j_{geo}), the anodic charge q^* (j_{spec}) and the applied Ir mass (j_{mass}). (c) Anodic charge q^* (reflecting the electrochemically active oxide surface area) measured by cyclic voltammetry between 0.4 and 1.4 V with 50 mV s^{-1}. (d) Amount of dissolved Ir during 30 min of OER with 1 mA cm^{-2}. The amount of dissolved Ir is provided normalized to the geometric surface area and to q^*.

the fraction of Ir atoms substituted by Ni (in at%) in the as-prepared mixed oxide.

Electrocatalytic OER Activity and Ir Dissolution. The electrocatalytic OER performance of the MO film catalysts was explored using the rotating disk electrode (RDE) technique. Figure 1a depicts quasi-stationary OER polarization curves of pure Ir oxide and MO catalysts. Clearly, mixing Ir and Ni in form of an oxide exhibits a tremendously beneficial effect on the electrocatalytic OER activity yielding in catalyst materials that, judged by their current density at a given overpotential, significantly exceed the catalytic activity of pure Ir oxide. Pure NiO is not shown in Figure 1a due to its poor OER activity in perchloric acid (see Figure S1).

Catalytic OER current densities at a fixed overpotential of 300 mV (1.530 V_{RHE}) are plotted and compared in Figure 1b as measure for the OER performance. Therein, the geometric and the Ir mass based current density exhibit a volcano type curve with a maximum at high Ni contents (67–79 at%). Compared to the Ir oxide reference catalyst the OER performance was improved by a factor of ∼8, based on the geometric current density (j_{geo}), or even more remarkably, by a factor of ∼20, based on the Ir mass based current density (j_{mass}). In other words, using Ir–Ni mixed oxides, the Ir amount of a water splitting anode catalyst could be reduced by a factor of 20 while maintaining the identical OER rate at the same electrode potential. Finally, in order to explore the origin of the tremendous improvement in OER activity, the surface specific OER activity was determined. The established method for the determination of the active Ir oxide surface area makes use of the anodic charge q* obtained in a fixed potential range (0.4–1.4 V_{RHE}) as measure proportional to the active Ir oxide area.[26−28] Experimental q^*-values are plotted in Figure 1c; they exhibit a maximum at intermediate Ni contents, indicating that 39%Ni and 67%Ni-MO showed the largest active oxide surface areas. The surface specific catalytic current density (current normalized by q^*) again increase with the Ni content up to 67%Ni-MO (see Figure 1b), but levels off at higher Ni contents within the accuracy of the measurement. Compared to pure Ir oxide, the surface specific OER activity of samples with an initial Ni content at and above 67 at% was increased by a factor of about 2.6.

Besides the electrocatalytic activity, the stability is the other major issue of OER catalysts.[3] Here the stability of Ir against dissolution was measured using potential-resolved online ICP-MS analysis[18,29] on samples which previously underwent the electrocatalytic OER protocol (*x*%Ni-MO-OER). In Figure 1d, the total mass of dissolved Ir during 30 min galvanostatic water electrolysis at 1 mA cm^{-2} is shown as a function of the initial Ni content. For our stability discussion, the dissolved Ir mass was normalized to the geometric (black) as well as the active (red) catalyst area (reflected by q^*). Looking at the geometric stability, the amount of dissolved Ir first increased with increasing Ni content and peaked at 79%Ni-MO. At this maximum the Ir dissolution rate is approximately 47 times higher than that of pure Ir oxide, while in the case of 67%Ni-MO it is 34 times higher. Although this appears to be a substantial drop in Ir stability relative to pure Ir oxide, we note that even the least stable thermally prepared MO film catalyst

DOI: 10.1021/jacs.5b07788
J. Am. Chem. Soc. 2015, 137, 13031−13040

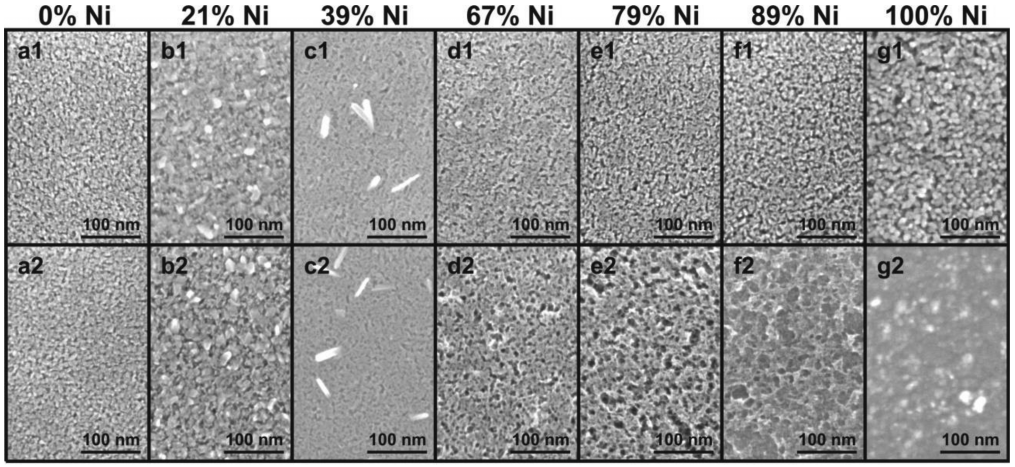

Figure 2. Top view SEM images of Ir−Ni mixed oxide films on Ti substrates with different initial Ni contents acquired on as prepared samples (MO-ap, upper row, a1−g1) and samples that underwent the OER protocol (MO-OER, bottom row, a2−g2).

of this study exhibits an Ir dissolution rate that is comparable to that of electrochemically oxidized Ir metal, and even much lower than that of electrochemically oxidized Ru metal.[18] Interestingly, geometric OER performance and geometric Ir dissolution rate peak at different Ni contents. Furthermore, 21%Ni-MO-OER showed a dissolution rate 14 times higher than that of pure Ir oxide, although the geometric OER activity was rather similar. Both observations indicate that OER activity and stability are not directly anticorrelated, which is supported by a comparative plot of OER activity and dissolved Ir amount (see Figure S2a). To show this more clearly, when the amount of dissolved Ir is normalized to the electrochemically active Ir oxide surface area (reflected by q^*) a broad plateau appears at Ni contents ≤67 at% (red balls in Figure 1d). The data in Figure 1b and d evidence that, although the surface specific Ir dissolution rate is rather constant across the plateau, the surface specific OER activity can be tuned and increases with the Ni content (compare Figure S2b). This provides further evidence for the principle possibility of decoupling OER activity and stability implying the existence of distinct material properties relevant to activity and stability.

Electrochemical Ni Dissolution, Compositional, and Morphological Stability. To uncover macroscopic and microscopic materials properties controlling the observed OER activity and Ir dissolution a wide range of scattering, spectroscopic, and microscopic characterization techniques were applied to the as-prepared Ir−Ni mixed oxide samples (referred to as MO-ap) and to Ir−Ni mixed oxide samples that had undergone OER catalysis (MO-OER).

Scanning electron micrographs of MO-ap and MO-OER, depicted in Figure 2, revealed morphological changes of the catalysts after OER. MO-ap samples generally consisted of dense, grained films with a certain apparent porosity and comparable film thicknesses in the 41 to 58 nm range (see cross-sectional studies in Figure S3). 0%Ni-MO-ap and 21%Ni-MO-ap were composed of very fine grains. For catalysts with higher Ni contents individual grains are hardly visible, but the films still revealed an apparent porosity. Instead, some needle-shaped presumably IrO_2 crystals segregated to the surface of the 39%Ni-MO-ap.

After OER, catalysts with ≤39 at% initial Ni content remained morphologically stable, while the others showed increasing sponge like porosity with increasing initial Ni content. This observation suggests that Ni was more and more leached out. In the case of the 100%Ni-MO-OER film its initial nanocrystalline structure vanished after OER due to heavy corrosion.

To understand the Ni leaching, bulk and near surface composition of MO-ap and MO-OER catalysts were determined and plotted against the initial Ni content, see Figure 3a. The bulk Ni content was determined by averaging XPS sputter depth profiles (solid triangles) and for MO-ap additionally by ICP-OES. Both approaches are in excellent agreement for MO-ap, validating the approach of XPS sputter depth profile averaging for bulk Ni content determination. After OER catalysis, bulk and surface Ni content (red symbols) evidence strong, yet incomplete Ni dissolution. For initial Ni contents ≤ 67 at%, residual Ni values surprisingly leveled at around 12 at%, likely stabilized through interaction with Ir. In fact, Ni dissolution rates obtained from online ICP-MS analysis were then in the same range as Ir dissolution rates (see Figure S4) reflecting the relative stability of remaining Ni in the leached oxides. This observation is important, as it demonstrates that about 12 at% Ni can be stabilized in the mixed oxide matrix and may contribute to electronic and geometric effects beneficial for the water splitting catalysis.

XPS sputter depth profiles of Ir and Ni of MO-OER and MO-ap catalysts are depicted in Figures 3b and S5. For the as-prepared catalysts, the Ni content is basically constant across the entire film depth (Figure S5), consistent with homogeneous Ir−Ni mixed oxides. Interestingly, after OER catalysis, rather constant Ni contents across the film depth were also observed up to 67 at% initial Ni content, although a large portion of Ni was leached out (Figure 3b). A Ni gradient clearly became apparent for 79%Ni-MO-OER, although it emerged already for 67%Ni-MO-OER. The 89%Ni-MO-OER film was too thin and too porous to obtain a meaningful depth profile measurement. However, the depth profile measurements demonstrate a surprisingly homogeneous Ni leaching across large distances up to 67 at% initial Ni content, precluding mass transport control of the dissolution process and instead highlighting the formation of Ir−Ni oxide interactions.

Atomic Structure of Ir−Ni Mixed Oxides. Grazing incidence X-ray diffraction (GI-XRD) was used to probe the crystallinity and to conduct a phase analysis of the MO-ap films. Data in Figure S6 suggested that all films were X-ray

DOI: 10.1021/jacs.5b07788
J. Am. Chem. Soc. 2015, 137, 13031−13040

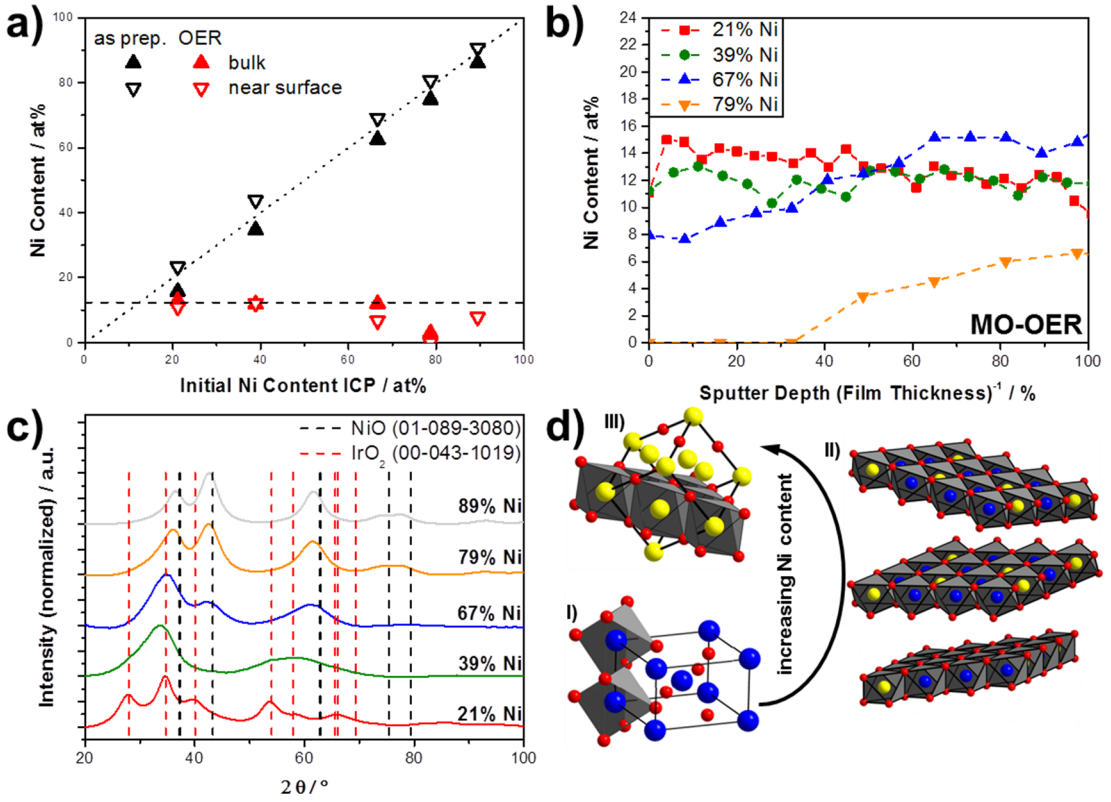

Figure 3. (a) Near surface and bulk composition of Ir−Ni mixed oxide films before (MO-ap) and after (MO-OER) the electrocatalytic OER protocol. The Ni content measured by ICP-OES is provided on the *x*-axis. The near surface Ni content and the bulk Ni content, shown on the *y*-axis, were determined by XPS or, respectively, by averaging XPS depth profiles. (b) XPS sputter depth profile measurements of MO-OER. (c) Integrated and baseline corrected selected area electron diffraction measurements of MO-ap transformed into the 2θ scale (Cu Kα). Reference patterns from the powder diffraction file are provided for comparison. (d) Structural model according to (c). (I) depicts the rutile type (IrO_2), and (III) the bunsenite type (NiO) unit cell. (II) depicts a structural model for 39%Ni-MO-ap. (O or OH, red; Ni, yellow; Ir, blue).

amorphous, except pure Ir and Ni oxide as well as the 21%Ni-MO-ap. The pure Ni oxide film formed a single rock-salt-type *bunsenite* phase. A rutile-type phase was detected for pure Ir oxide and the 21%Ni-MO-ap film. To further investigate the structure of the MO-ap films at the nanoscale, selected area electron diffraction (SAED) was employed; see Figure 3c. Now, all MO-ap samples showed clear diffraction patterns suggesting nanocrystallinity. Consistent with the GI-XRD data, a rutile type phase was identified for 21%Ni-MO-ap. The structure of the next higher Ni content catalyst, the 39%Ni-MO-ap, however, changed drastically. Rutile-type reflections vanished in favor of new reflections at approximately 34° and 60° 2θ. With further increasing Ni content an additional reflection at approximately 42.5° evolved and grew in intensity with increasing Ni content. This was accompanied by shifts of the 34° and 60° reflections, until the pattern of an expanded bunsenite type structure evolved for the 89%Ni-MO-ap catalyst film.

These findings can be fully accounted for considering brucite like layered structures characterized by layers of edge-sharing Ni−O octahedra. Similar structures are commonly observed for Ni hydroxides and oxy-hydroxides, whereby the difference largely consists in the arrangement of the brucite like Ni−O layers along the *c* axis.[30,31] Consistent with missing crystalline order between the layers in the 39%Ni-MO-ap catalyst, Figure 3d II depicts a structural model composed of misaligned, turbostratic Ni−O layers with brucite like layer structure. With increasing Ni content the Ni−O layers become more and more interconnected yielding in a three dimensionally ordered structure as seen by the growth of the bunsenite reflection at ~42.5°. One Ni−O brucite like layer is highlighted in the bunsenite unit cell in Figure 3d,III. The continuous downshift of the ~34° and ~60° reflections with decreasing Ni content indicates a lattice expansion due to the increased incorporation of larger Ir ions. The continuity of the structural changes strongly suggest the presence of one mixed oxide phase in each catalyst other than the pure oxides and, possibly, the 21%Ni-MO-ap, where the intense reflections of the rutile-type phase may impede the resolution of mixed oxide reflections.

Electronic Band Structure and Surface Chemical State of Ir−Ni Mixed Oxides. To get insight in the electronic structure and the surface chemical states of the Ir−Ni oxide thin films before and after OER catalysis, X-ray absorption and X-ray photoemission studies were conducted and compared to theoretical calculations. Figure 4a and b depict the O K-edge X-ray absorption spectra of MO-ap and MO-OER, wherein O 1s electrons are excited to unoccupied states probing the *local unoccupied O 2p density of states*, the fine structure of which is determined by mixing with metal states.[32] Clearly, the spectra after OER catalysis revealed substantial differences to the as-prepared state (compare Figure 4b and a), which can be understood at an atomic orbital level when combined with quantum chemical computations.

To understand and predict the experimental O K-edge spectra we used density functional theory (DFT) at the PBE+U level for IrO_2 and NiO. A linear response approach was used to compute the Hubbard U for Ni[33] (for Ir U was set to zero, see the SI for details). These calculations are in good agreement

DOI: 10.1021/jacs.5b07788
J. Am. Chem. Soc. 2015, 137, 13031−13040

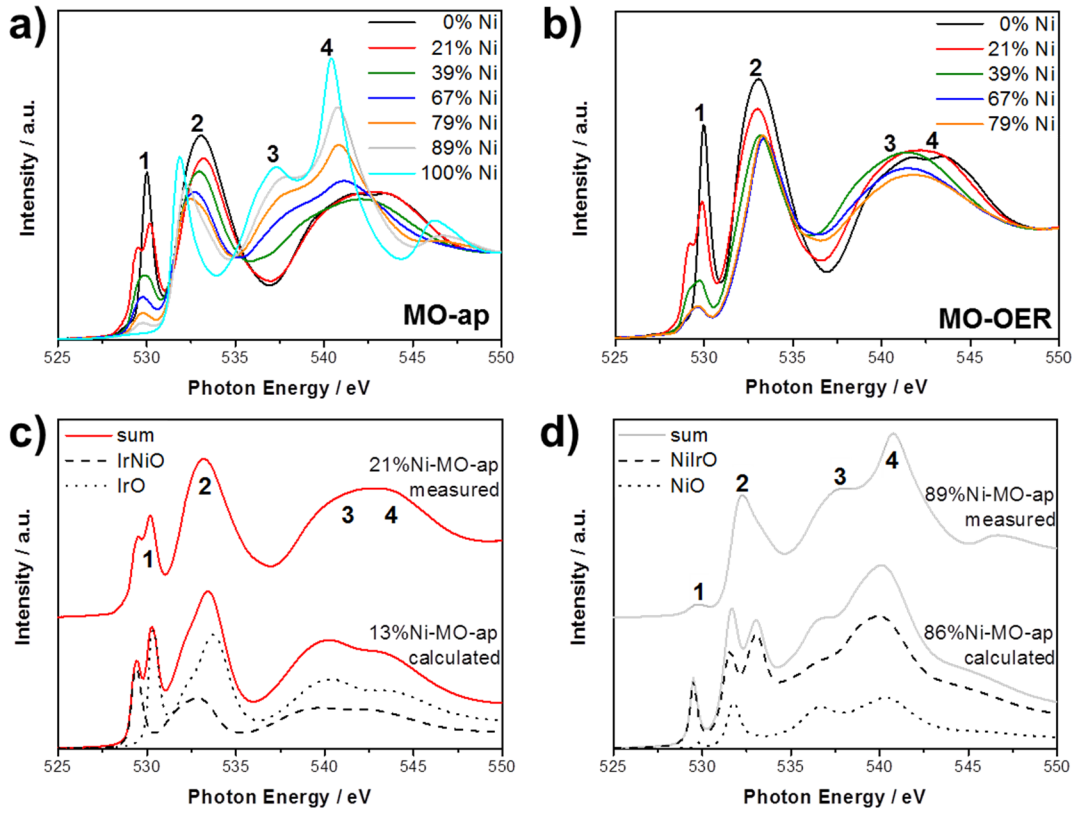

Figure 4. O K-edge absorption spectra of Ir−Ni mixed oxide films (a) in the as-prepared state (MO-ap) and (b) after OER catalysis (MO-OER). Comparison of calculated and measured O K-edge absorption spectra of MO-ap with (c) low Ni content (calculated, 13%Ni-MO-ap; measured, 21% Ni-MO-ap) and (d) high Ni content (calculated, 86%Ni-MO-ap; measured, 89%Ni-MO-ap).

with the measured spectra (see the SI). The experimental peak 1 present for IrO_2 but absent for NiO can be assigned to excitation into states that are nominally M-O (M: Ir or Ni) π antibonding in character. Since these states are filled for NiO, peak 1 is absent in this case. Peak 2, present for pure Ir and Ni oxide, is assigned to transitions into O 2p states that can be considered M-O σ antibonding in character. Peaks 3 and 4 are due to excitations into O 2p states hybridized with M-sp states, as expected from previous work for NiO.[33]

To gain atomic-level insight into the O K-edge spectrum of the low Ni content MOs we performed DFT calculations on a rutile IrO_2 in which every eighth Ir atom is substituted by Ni (see the SI), yielding 13%Ni-MO. This structure displays two kinds of distinctly coordinated oxygen atoms, one coordinated by Ir atoms only and one coordinated by Ir and Ni atoms (see the SI). The contribution of these oxygen atoms is shown separately in Figure 4c. The low energy component of peak 1 is related to oxygen coordinated by Ir and Ni, more specifically to O 2p states involved in Ir−O and Ni−O π antibonding. The higher energy component of peak 1 is assigned to Ir−O π antibonding states relatively unperturbed by Ni. Peak 2 is due to transitions into O 2p states involved in Ir−O and Ni−O σ antibonding. Similarly to the low Ni content, the high Ni content samples were modeled starting from a bunsenite type Ni oxide in which every eighth Ni atom was substituted by Ir, resulting in 86%Ni-MO (see the SI). Again, two kinds of distinctly coordinated oxygen atoms exist. The calculations suggest that the small experimental peak 1 can be attributed to oxygen coordinated by Ir and Ni, more precisely to absorptions into Ir−O π antibonding states, while peak 2 is due to transitions into Ni−O and Ir−O σ antibonding states (see Figure 4d and SI). Similar to the case of the pure oxides, peaks 3 and 4 in the mixed oxides are assigned to absorptions into O 2p states hybridized with metal s and p levels. The excellent agreement between calculations and experiments verifies the structural model and thus the presence of mixed oxides in the as prepared state.

X-ray absorption spectra of the samples after OER catalysis are provided in Figure 4b. The spectra of 89%Ni and 100%Ni-MO-OER are not included, since oxygen species stemming from the oxidized Ti substrate contributed significantly to these spectra. This was because extensive Ni leaching rendered the remaining MO-OER film porous and as a result of this it did no longer sufficiently cover the substrate. Interestingly, after OER catalysis, peak 2 shifted to photon energies higher than those of pure Ir oxide and peak 1 shifted slightly to lower photon energies. While our DFT calculations suggest that the shift of peak 2 might be related to OH species formed due to Ni leaching (see the SI), they do not account for the shift of peak 1. Thus, the shift of peak 1 indicates changes in the metal−oxygen bonding situation invoked by Ni leaching.

X-ray photoelectron spectroscopy was used to characterize the chemical state of Ir, Ni and O in MO-ap and MO-OER film catalysts. Figure 5a depicts the Ni 2p region of MO-ap catalysts. The pure Ni oxide spectrum showed binding energy and line shape closely resembling to a NiO reference material.[34] Line shapes and binding energies for all MO-ap are essentially similar to the pure Ni oxide film. However, the signals at ~854 eV (p1) and ~856 eV (p2) showed a varying intensity ratio depending on the Ni content. As pointed out by Alders et al. the intensity of p2 relative to p1 in NiO is a function of the local environment around the Ni atoms.[35] Thus, the observed

DOI: 10.1021/jacs.5b07788
J. Am. Chem. Soc. 2015, 137, 13031−13040

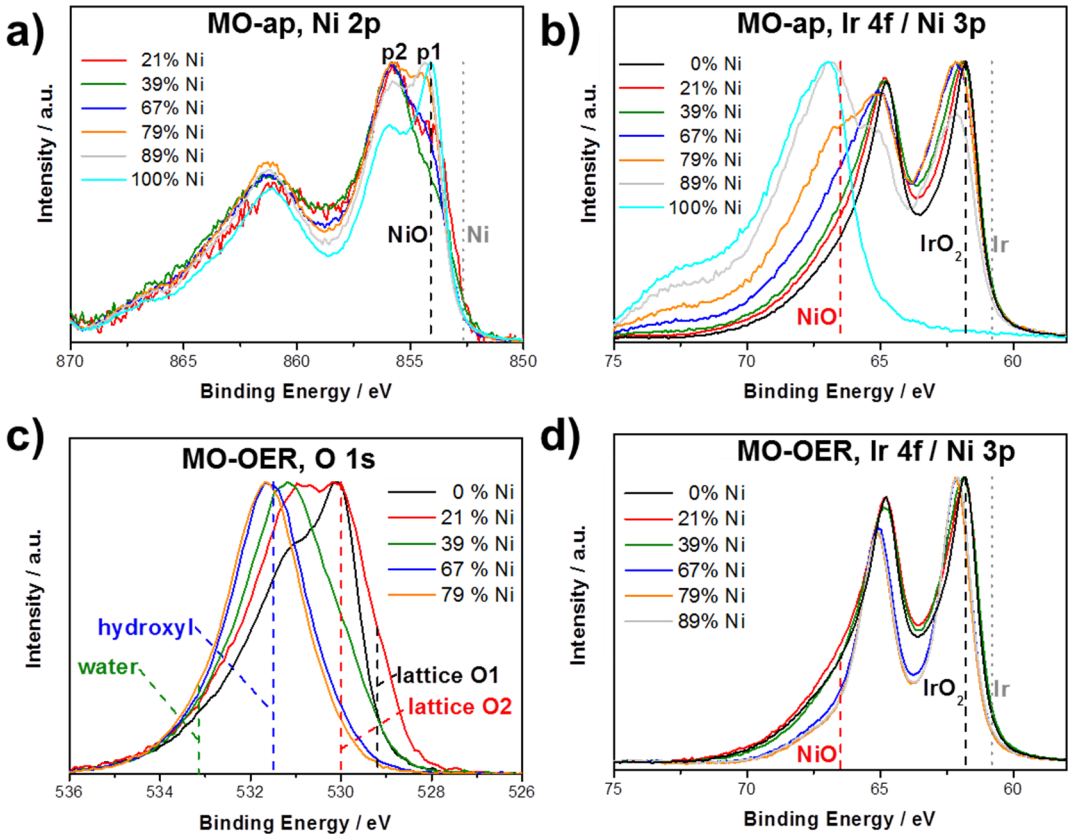

Figure 5. X-ray photoelectron spectra provided together with reference binding energies. Ni 2p region measured on as prepared Ir−Ni oxide films (MO-ap, a). Ir 4f and Ni 3p region measured on as prepared (MO-ap, b) and electrochemically treated (MO-OER, d) films. O 1s region measured on electrochemically treated films (MO-OER, c). Reference binding energies: Ir,[36] IrO_2,[37] Ni,[38] NiO,[39] and oxygen species.[25]

variation of the p1/p2 intensity ratio likely indicates changes of the local Ni environment dependent on the Ni content, as expected for mixed oxides with different Ir:Ni ratios. XPS line shape and binding energy of the catalytically tested thin films (MO-OER) in the Ni 2p region remained largely unchanged, see Figure S15, but p1 almost disappeared consistent with a dramatic change in local Ni coordination environment due to Ni leaching.

For the MO-ap catalyst films, Ir XPS studies are somewhat complicated to analyze due to the overlap of Ir 4f and Ni 3p signals, see Figure 5b. The spectra of the Ni leached MO-OER catalysts, however, are largely dominated by Ir; see Figure 5d. The as-prepared pure Ir oxide film showed an Ir 4f doublet with an asymmetric peak shape and a binding energy coinciding a value previously observed for IrO_2.[37] As recently pointed out by Kahk et al., the asymmetric peak shape is due to final state screening and, therefore, to the metallic character of IrO_2. However, the actual screening process is not yet fully understood.[40] In order to obtain more detailed chemical information about Ir in MO-ap and resolve Ir from Ni signals, extensive curve fitting was applied (see Figures S17 and S18). Unlike pure Ir oxide, the 4f peak width of the MO-ap increased with increasing Ni content and required a second Ir component in order to obtain a reasonable fit quality. Note that without this second Ir 4f component we were unable to account for the doublet area ratio. The increased peak width indicated a variation in the local surroundings of the Ir centers due to perturbation of Ir oxide by Ni. Upon Ni leaching, the signal width decreased supporting this interpretation. Interestingly, beside the width, the line shape of the Ir 4f signals in MO-ap and MO-OER samples differs depending on the initial Ni content, which can be traced directly in Figure 5d for MO-OER or, respectively, in the fits (see Figure S17) for MO-ap. For low initial Ni contents $\lesssim$39 at% in MO-OER the Ir signals are characterized by a pronounced asymmetry, which is reduced at higher initial Ni contents. Since the peak asymmetry is related to the metallic character the reduced asymmetry indicates a reduced metallic character. Although Ni was leached out to a large extent, the asymmetric line shape of IrO_2 did not reemerge in the leached MO-OER catalysts with initial Ni contents $\geq$ 67 at%.

The O 1s spectra of the catalysts prior and after OER testing are depicted in Figures S16 and 5c, respectively. Fits of the O 1s spectra (Figures S19 and S20) revealed up to 4 different oxygen species at about 529.2, 529.9, 531.4, and 533.1 eV. The species at ~533.1 eV can be assigned to adsorbed water, whereas the species at 529.9 and 531.4 eV are related to lattice oxygen and hydroxyl groups, respectively.[25,41] The species at 529.2 eV appeared with mixed oxides, being particularly visible in 21%Ni-MO, and our DFT calculations indicated that lattice oxygen atoms bridging Ir and Ni atoms have an O 1s binding energy in this range. The binding energy of lattice oxygen in the metal oxides is a weak function of the Ni content, and thus that of pure NiO is located at 529.6 eV. Figure 6a depicts the fraction of surface hydroxyl species (OH-fraction) to the surface oxide related species (OH and both lattice oxygen species). In MO-ap, the OH-fraction was just a weak function of the Ni content. Interestingly, after Ni leaching and OER catalysis the OH fraction increased depending on the initial Ni content. Pure Ir oxide showed almost no change in the OH fraction, while films

DOI: 10.1021/jacs.5b07788
J. Am. Chem. Soc. 2015, 137, 13031−13040

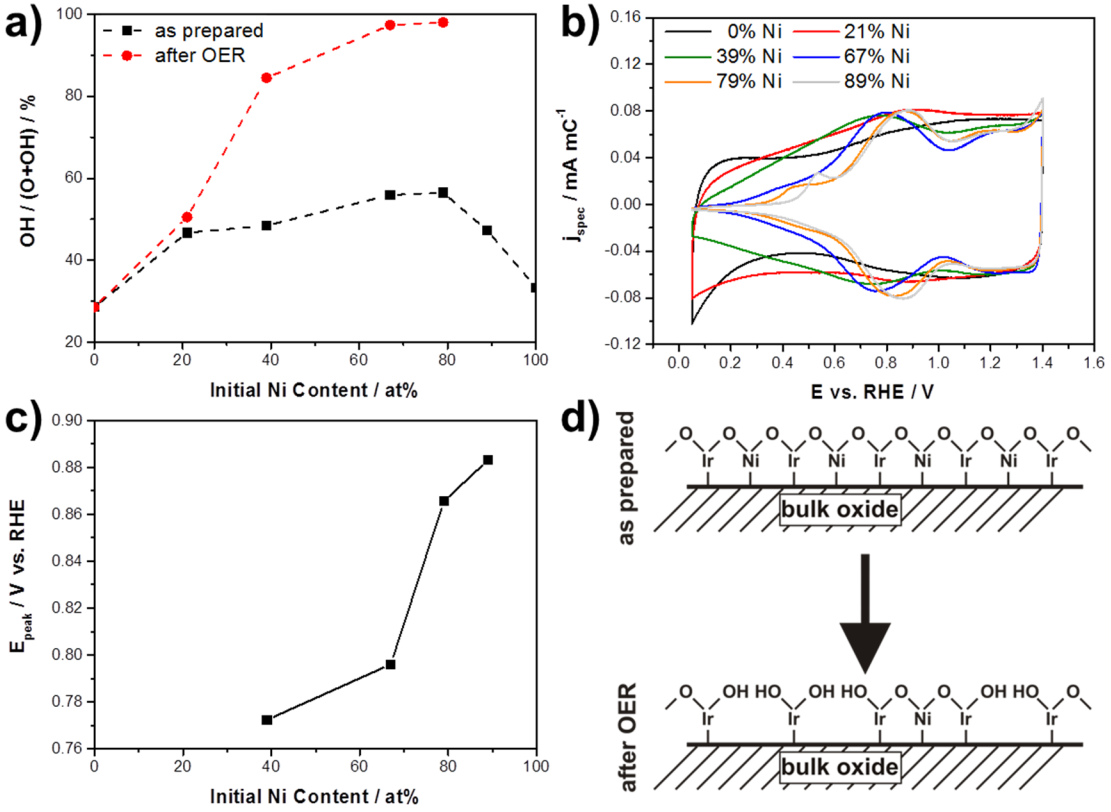

Figure 6. (a) Hydroxyl group (OH) fraction to the total oxide related oxygen (hydroxyl groups and both lattice oxygen species) as determined by XPS. (b) Cyclic voltammetry measured with 50 mV s^{-1}. The current was normalized to q^* (reflecting the electrochemical active oxide surface area). (c) Potential of the anodic peak observed in (b). (d) Model of Ni leaching from the surface of Ir–Ni mixed oxides.

with higher initial Ni contents showed an increased OH fraction. The OH fraction of MO-OER films increased with increasing initial Ni content, until a value close to 100% was reached for 67%Ni-MO-OER. Similar to XAS measurements for MO-OER, no OH fraction could be obtained for 89%Ni-MO-OER and the pure Ni oxide film due to the detection of Ti oxide.

The Surface Electrochemistry of Ir–Ni Mixed Oxide Catalysts. To get insight into the surface electrochemical redox processes, cyclic voltammetry (CV) was measured within the OER protocol after the first OER polarization curves. Figure 6b evidence dramatic changes in the surface electrochemistry depending on the initial Ni content. While pure Ir oxide exhibited its characteristic reduction feature close to 0 V_{RHE} followed by an indistinct broad redox wave between 0.4 and 1.4 V_{RHE},[25,42,43] higher Ni contents resulted in the disappearance of the reduction feature, yet associated with a new distinct redox feature around 0.8 V_{RHE}. At Ni contents ≥ 67 at%, this feature was accompanied by a low-potential shoulder. Interestingly, these features are commonly observed for *electrochemically prepared so-called hydrous* Ir oxides, where the main peak at ~0.8 V_{RHE} could be attributed to the Ir(III)/Ir(IV) transition.[4,20,44] Overall, the thermally prepared Ir–Ni mixed oxide catalysts with initial Ni contents ≥39 at% displayed a surface redox chemistry that was much more similar to electrochemically prepared than to thermally prepared Ir oxides. In Figure 6c, the oxidation peak potentials of Ir(III)/Ir(IV) are plotted for each catalyst over its initial Ni content. Clearly, the Ir redox potential strongly correlates with the initial Ni content, evidencing an anodic shift in redox potential (for ≥39 at% Ni), which indicates a stabilization of the lower relative to the higher Ir oxide.

Structure–Reactivity Correlations and Catalytic Performance Descriptors. The goal of the present study is a deeper understanding of the electrochemical OER on Ir–Ni mixed oxide model catalysts, which will aid in the development of improved PEM electrolyzer and PEC anodes. Our data evidence that Ir–Ni mixed oxide film catalysts offer the opportunity to continuously tune the OER activity and stability within a bimetallic system by varying a single synthesis parameter, that is, the composition. What sets this study apart from previous bimetallic oxide OER studies is our effort to identify microscopic and macroscopic parameters that are responsible for the continuous variation of the OER performance and, thus, represent controlling parameters for the electrocatalytic OER activity and stability. This approach offers a deeper understanding of the OER on the chosen Ir–Ni mixed oxide catalysts. In the following, we now establish correlations between the trends in structure, activity, and stability.

First we address the role of Ni as a sacrificial catalyst component and the implication of Ni leaching for the active catalyst structure. The prepared MO-ap films were predominantly single phase homogeneous Ir–Ni mixed oxides in which the formation of a rutile-type structure was largely suppressed in favor of a layered brucite like structure. Ni was leached from these oxides during the electrocatalytic OER protocol, yielding in Ir-rich oxides. As a result, the tested MO-OER films became more porous, and, on an atomic scale, the binding environment of oxygen was significantly altered. In this Ni-depleted catalytically active state, the remaining Ir-rich oxide must react structurally to compensate the Ni loss. A schematic

DOI: 10.1021/jacs.5b07788
J. Am. Chem. Soc. 2015, 137, 13031–13040

hypothetical model for this is provided in Figure 6d, which helps to rationalize the geometric, compositional, and electronic transformations during the catalyst leaching and activation.

When Ni is leached from MO-ap films, oxygen atoms lose binding partners, which is expected to weaken the binding strength of the Ni-depleted oxygen atoms to the oxide lattice. To further ensure electroneutrality, the Ni-depleted oxygen atoms will take up protons from the electrolyte and, thus, form surface hydroxyl groups, as indicated in Figure 6d. Indeed, upon Ni leaching the surface OH fraction increased significantly up to 67 at% initial Ni content (Figure 6a). Importantly, the surface-specific OER activity revealed a rather similar trend as the OH fraction: Both increase with increasing Ni content and reach saturation at 67 at% Ni. Thus, we conclude that the ratio of weakly bonded surface hydroxyls is directly related to the surface specific catalytic OER activity of Ir oxides. This trend becomes intuitive if surface OH groups are assumed to act as reactive surface intermediates on active sites of the catalytic process. Thus, we conclude that the leaching of Ni atoms acts as promoter for the formation of structurally flexible, reactive OH groups, while reducing the less reactive oxide surface termination involving stable, unreactive divalent =O surface oxygen species.

To put our conclusions in the context of a chemical reaction mechanism, we refer to a recent OER reaction model.[45,46] This mechanism puts forward the water-assisted stepwise deprotonation of hydroxyl groups forming reactive peroxide species, which are then released from the active site to form molecular oxygen. The overall process was predicted to proceed at a reasonable rate only if the surface intermediates, including OH groups, display a balanced binding to the oxide lattice. Bulk lattice oxygen species binding much stronger than OH groups, such as bridged lattice O or terminal =O groups, are expected to be bounded too strongly and are therefore not expected to participate directly in the OER process. Our findings are in line with results by Fierro et al. that part of the evolved oxygen actually originates from the Ir oxide catalyst itself, most likely through involvement of its loosely bound surface OH groups.[47] Although terminal hydroxyl groups show nominally higher XPS binding energies than other surface oxygen species, their chemical bond strength varies strongly with local coordination. Still, the OH groups with optimal balanced binding energy would always dominate the overall OER reaction rate. Implications for changes of the oxygen binding strength were found by XAS at the O K-edge and CV.

In regard to possible Ni-related oxide lattice geometry and strain effects, we point out that a strong increase in the surface specific catalytic water splitting activity occurred at essentially constant residual Ni ratios of about 12 at% Ni in the active oxide films (for initial Ni contents $\leq$ 67 at%). This is in contrast to Ni-leached bimetallic PtNi alloy catalysts where residual subsurface Ni atoms gave rise to surface lattice strain effects on the catalytic activity.[48] We therefore conclude that the residual near-surface Ni ratio is not a suitable quantitative descriptor for OER activity, and oxide lattice strain effects are likely of limited significance. This conclusion does not preclude that the presence of some residual Ni may be critical to structurally support the active films. The fact that 79%Ni-MO still exhibited improved intrinsic OER activity over pure Ir oxide although the residual Ni content was far below 12 at% suggests further evidence for the critical role of the formation and presence of specific and possibly reactive oxygenated surface species.

Finally, the stability against dissolution of surface Ir ions in the mixed oxide lattice depends plausibly on the strength and the number of Ir−O−M (M: Ir or Ni) binding motifs. Following our schematic model in Figure 6d, the number of such motifs in catalytically active Ir-enriched MOs decreases with higher initial Ni content, as more Ni atoms can and will be leached out. Thus, Ir dissolution should increase with initial Ni content. Indeed, this trend was observed experimentally. We conclude and predict that a stable and active Ir oxide water splitting OER catalyst combines the highest possible number of reactive surface hydroxyl groups with the highest possible number of intact Ir−O−M binding motifs in the subsurface.

4. CONCLUSIONS

Mixed bimetallic oxides offer great opportunities for a systematic tuning of electrocatalytic activity and stability. This is exemplified here using well-defined thermally prepared Ir−Ni oxide thin films catalyzing the oxygen evolution reaction under acidic conditions similar to PEM electrolyzers or PEC devices. First, we have shown that Ir−Ni mixed oxides offer an unprecedented 20-fold improvement in Ir mass-based water splitting OER activity over state-of-art pure Ir oxide catalysts. Similarly, activity improvements were observed on a geometric as well as on an active surface area basis.

Beyond the activity improvement, we have placed much emphasis on a more fundamental characterization and description of the catalysts, their performance and their stability. To this end, we have studied the geometric, electronic, and morphological structure of the various Ir−Ni mixed oxide catalysts. We accomplished a number of novel correlations between activity and stability and microscopic descriptors and managed to reject others such as Ni-related geometric strain effects.

Our data and analysis have resulted in a simple, yet intuitive model for the formation of the active state of the catalytic surface. The model suggested that the coverage of reactive surface hydroxyls serves as a useful descriptor for OER activity. Formed by initial Ni dissolution and disruption of Ir−O−M motifs, the surface hydroxyls showed a reduced binding to the oxide lattice, which was conducive to catalytic activity. Though stability of Ir atoms was compromised in this process as well, surface normalized dissolution of Ir did not correlate with catalytic activity, suggesting, contrary to common belief, that a separate optimization of activity and stability may actually be possible. We further established that thermally prepared yet Ni-leached Ir−Ni oxide film catalysts exhibited compositional stability and surface electrochemical redox characteristics that closely resembled those of Ir oxides formed via electrochemical oxidation of metallic Ir surfaces. Hence, we demonstrated how to balance catalytic activity advantages of oxidized metals with stability benefits of thermally prepared bulk oxides.

In more general terms, this study highlights the opportunities offered by Ir−Ni bimetallic oxides to tune their catalytic stability and activity at anodes in highly corrosive acidic environments. We are confident that our results will serve as inspiration for the design of other mixed oxide catalysts for similar anodic electrode processes, such as the electrocatalytic synthesis of industrial gases.

DOI: 10.1021/jacs.5b07788
J. Am. Chem. Soc. 2015, 137, 13031−13040

■ ASSOCIATED CONTENT

Supporting Information

The Supporting Information is available free of charge on the ACS Publications website at DOI: 10.1021/jacs.5b07788.

Further experimental details, additional electrochemical data, film-thickness measurements, Ni dissolution measurements, additional XPS sputter depth profiles, grazing incidence X-ray diffraction measurements, additional XP spectra including fits and further details concerning the DFT calculations (PDF)

■ AUTHOR INFORMATION

Corresponding Authors

*pstrasser@tu-berlin.de

*tobias.reier@tu-berlin.de

Notes

The authors declare no competing financial interest.

■ ACKNOWLEDGMENTS

Financial support by the German Research Foundation (DFG) under the Priority Program 1613 is gratefully acknowledged. This work received funding from the German Federal Ministry of Education and Research (Bundesministerium für Bildung und Forschung, BMBF) under the grant reference number 03SF0433A. We thank the HZB for allocation of synchrotron radiation beamtime and Dr. Kraehnert for providing access to a scanning electron microscope.

■ REFERENCES

(1) Dau, H.; Limberg, C.; Reier, T.; Risch, M.; Roggan, S.; Strasser, P. *ChemCatChem* **2010**, *2*, 724.

(2) Carmo, M.; Fritz, D.; Mergel, J.; Stolten, D. *Int. J. Hydrogen Energy* **2013**, *38*, 4901.

(3) Katsounaros, I.; Cherevko, S.; Zeradjanin, A. R.; Mayrhofer, K. J. J. *Angew. Chem., Int. Ed.* **2014**, *53*, 102.

(4) Reier, T.; Oezaslan, M.; Strasser, P. *ACS Catal.* **2012**, *2*, 1765.

(5) Ardizzone, S.; Bianchi, C. L.; Cappelletti, G.; Ionita, M.; Minguzzi, A.; Rondinini, S.; Vertova, A. *J. Electroanal. Chem.* **2006**, *589*, 160.

(6) Comninellis, C.; Vercesi, G. P. *J. Appl. Electrochem.* **1991**, *21*, 335.

(7) Ortel, E.; Reier, T.; Strasser, P.; Kraehnert, R. *Chem. Mater.* **2011**, *23*, 3201.

(8) Oh, H. S.; Nong, H. N.; Strasser, P. *Adv. Funct. Mater.* **2015**, *25*, 1074.

(9) Terezo, A. J.; Bisquert, J.; Pereira, E. C.; Garcia-Belmonte, G. *J. Electroanal. Chem.* **2001**, *508*, 59.

(10) Chen, G.; Chen, X.; Yue, P. L. *J. Phys. Chem. B* **2002**, *106*, 4364.

(11) De Pauli, C. P.; Trasatti, S. *J. Electroanal. Chem.* **2002**, *538*−*539*, 145.

(12) Zhang, J.-J.; Hu, J.-M.; Zhang, J.-Q.; Cao, C.-N. *Int. J. Hydrogen Energy* **2011**, *36*, 5218.

(13) Macounová, K.; Jirkovský, J.; Makarova, M. V.; Franc, J.; Krtil, P. *J. Solid State Electrochem.* **2009**, *13*, 959.

(14) Forgie, R.; Bugosh, G.; Neyerlin, K. C.; Liu, Z. C.; Strasser, P. *Electrochem. Solid-State Lett.* **2010**, *13*, B36.

(15) Petrykin, V.; Bastl, Z.; Franc, J.; Macounova, K.; Makarova, M.; Mukerjee, S.; Ramaswamy, N.; Spirovova, I.; Krtil, P. *J. Phys. Chem. C* **2009**, *113*, 21657.

(16) Kötz, R.; Stucki, S.; Scherson, D.; Kolb, D. M. *J. Electroanal. Chem. Interfacial Electrochem.* **1984**, *172*, 211.

(17) Wohlfahrt-Mehrens, M.; Heitbaum, J. *J. Electroanal. Chem. Interfacial Electrochem.* **1987**, *237*, 251.

(18) Cherevko, S.; Zeradjanin, A. R.; Topalov, A. A.; Kulyk, N.; Katsounaros, I.; Mayrhofer, K. J. J. *ChemCatChem* **2014**, *6*, 2219.

(19) Frydendal, R.; Paoli, E. A.; Knudsen, B. P.; Wickman, B.; Malacrida, P.; Stephens, I. E. L.; Chorkendorff, I. *ChemElectroChem* **2014**, *1*, 2075.

(20) Nong, H. N.; Gan, L.; Willinger, E.; Teschner, D.; Strasser, P. *Chem. Sci.* **2014**, *5*, 2955.

(21) Nong, H. N.; Oh, H. S.; Reier, T.; Willinger, E.; Willinger, M. G.; Petkov, V.; Teschner, D.; Strasser, P. *Angew. Chem., Int. Ed.* **2015**, *54*, 2975.

(22) Cherevko, S.; Reier, T.; Zeradjanin, A. R.; Pawolek, Z.; Strasser, P.; Mayrhofer, K. J. J. *Electrochem. Commun.* **2014**, *48*, 81.

(23) Bergmann, A.; Zaharieva, I.; Dau, H.; Strasser, P. *Energy Environ. Sci.* **2013**, *6*, 2745.

(24) Giannozzi, P.; Baroni, S.; Bonini, N.; Calandra, M.; Car, R.; Cavazzoni, C.; Ceresoli, D.; Chiarotti, G. L.; Cococcioni, M.; Dabo, I.; Dal Corso, A.; de Gironcoli, S.; Fabris, S.; Fratesi, G.; Gebauer, R.; Gerstmann, U.; Gougoussis, C.; Kokalj, A.; Lazzeri, M.; Martin-Samos, L.; Marzari, N.; Mauri, F.; Mazzarello, R.; Paolini, S.; Pasquarello, A.; Paulatto, L.; Sbraccia, C.; Scandolo, S.; Sclauzero, G.; Seitsonen, A. P.; Smogunov, A.; Umari, P.; Wentzcovitch, R. M. *J. Phys.: Condens. Matter* **2009**, *21*, 395502.

(25) Reier, T.; Teschner, D.; Lunkenbein, T.; Bergmann, A.; Selve, S.; Kraehnert, R.; Schlögl, R.; Strasser, P. *J. Electrochem. Soc.* **2014**, *161*, F876.

(26) Trasatti, S. *Electrochim. Acta* **1984**, *29*, 1503.

(27) da Silva, L. A.; Alves, V. A.; da Silva, M. A. P.; Trasatti, S.; Boodts, J. F. C. *Electrochim. Acta* **1997**, *42*, 271.

(28) Ardizzone, S.; Carugati, A.; Trasatti, S. *J. Electroanal. Chem. Interfacial Electrochem.* **1981**, *126*, 287.

(29) Cherevko, S.; Topalov, A. A.; Zeradjanin, A. R.; Keeley, G. P.; Mayrhofer, K. J. J. *Electrocatalysis* **2014**, *5*, 235.

(30) Delahaye-Vidal, A.; Beaudoin, B.; Sac-Epée, N.; Tekaia-Elhsissen, K.; Audemer, A.; Figlarz, M. *Solid State Ionics* **1996**, *84*, 239.

(31) Oliva, P.; Leonardi, J.; Laurent, J. F.; Delmas, C.; Braconnier, J. J.; Figlarz, M.; Fievet, F.; Guibert, A. d. *J. Power Sources* **1982**, *8*, 229.

(32) Suntivich, J.; Hong, W. T.; Lee, Y. L.; Rondinelli, J. M.; Yang, W. L.; Goodenough, J. B.; Dabrowski, B.; Freeland, J. W.; Shao-Horn, Y. *J. Phys. Chem. C* **2014**, *118*, 1856.

(33) Cococcioni, M.; de Gironcoli, S. *Phys. Rev. B: Condens. Matter Mater. Phys.* **2005**, *71*, 035105.

(34) Grosvenor, A. P.; Biesinger, M. C.; Smart, R. S. C.; McIntyre, N. S. *Surf. Sci.* **2006**, *600*, 1771.

(35) Alders, D.; Voogt, F. C.; Hibma, T.; Sawatzky, G. A. *Phys. Rev. B: Condens. Matter Mater. Phys.* **1996**, *54*, 7716.

(36) Powell, C. J. *J. Electron Spectrosc. Relat. Phenom.* **2012**, *185*, 1.

(37) Moser, M.; Mondelli, C.; Amrute, A. P.; Tazawa, A.; Teschner, D.; Schuster, M. E.; Klein-Hoffman, A.; López, N.; Schmidt, T.; Pérez-Ramírez, J. *ACS Catal.* **2013**, *3*, 2813.

(38) Mansour, A. N. *Surf. Sci. Spectra* **1994**, *3*, 211.

(39) Mansour, A. N. *Surf. Sci. Spectra* **1994**, *3*, 231.

(40) Kahk, J. M.; Poll, C. G.; Oropeza, F. E.; Ablett, J. M.; Céolin, D.; Rueff, J.-P.; Agrestini, S.; Utsumi, Y.; Tsuei, K. D.; Liao, Y. F.; Borgatti, F.; Panaccione, G.; Regoutz, A.; Egdell, R. G.; Morgan, B. J.; Scanlon, D. O.; Payne, D. J. *Phys. Rev. Lett.* **2014**, *112*, 117601.

(41) Grosvenor, A. P.; Kobe, B. A.; McIntyre, N. S. *Surf. Sci.* **2004**, *572*, 217.

(42) Reier, T.; Weidinger, I.; Hildebrandt, P.; Kraehnert, R.; Strasser, P. *ECS Trans.* **2013**, *58*, 39.

(43) Fierro, S.; Kapałka, A.; Comninellis, C. *Electrochem. Commun.* **2010**, *12*, 172.

(44) Conway, B. E.; Mozota, J. *Electrochim. Acta* **1983**, *28*, 9.

(45) Rossmeisl, J.; Qu, Z. W.; Zhu, H.; Kroes, G. J.; Nørskov, J. K. *J. Electroanal. Chem.* **2007**, *607*, 83.

(46) Halck, N. B.; Petrykin, V.; Krtil, P.; Rossmeisl, J. *Phys. Chem. Chem. Phys.* **2014**, *16*, 13682.

(47) Fierro, S.; Nagel, T.; Baltruschat, H.; Comninellis, C. *Electrochem. Commun.* **2007**, *9*, 1969.

(48) Cui, C. H.; Gan, L.; Neumann, M.; Heggen, M.; Cuenya, B. R.; Strasser, P. *J. Am. Chem. Soc.* **2014**, *136*, 4813.

DOI: 10.1021/jacs.5b07788
J. Am. Chem. Soc. 2015, 137, 13031−13040